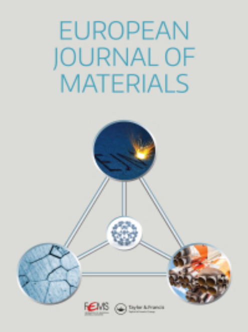

Taylor & Francis
Taylor & Francis Group

European Journal of Materials

ISSN: (Print) (Online) Journal homepage: https://www.tandfonline.com/loi/tems20

Micromechanical behavior of annealed Ti-6Al-4V produced by Laser Powder Bed Fusion

Tatiana Mishurova, Sergei Evsevleev, Katia Artzt, Jan Haubrich, Igor Sevostianov, Guillermo Requena & Giovanni Bruno

To cite this article: Tatiana Mishurova, Sergei Evsevleev, Katia Artzt, Jan Haubrich, Igor Sevostianov, Guillermo Requena & Giovanni Bruno (2022) Micromechanical behavior of annealed Ti-6Al-4V produced by Laser Powder Bed Fusion, European Journal of Materials, 2:1, 186-200, DOI: 10.1080/26889277.2022.2063763

To link to this article: https://doi.org/10.1080/26889277.2022.2063763

EUROPEAN JOURNAL OF MATERIALS
2022, VOL. 2, NO. 1, 186–201
https://doi.org/10.1080/26889277.2022.2063763

RESEARCH ARTICLE

OPEN ACCESS

Check for updates

Micromechanical behavior of annealed Ti-6Al-4V produced by Laser Powder Bed Fusion

Tatiana Mishurova[a], Sergei Evsevleev[a], Katia Artzt[b], Jan Haubrich[b], Igor Sevostianov[c], Guillermo Requena[b,d] and Giovanni Bruno[a,e]

[a]Bundesanstalt für Materialforschung und–prüfung (BAM; Federal Institute for Materials Research and Testing), Berlin, Germany; [b]Institute of Materials Research, German Aerospace Center (DLR; Deutsches Zentrum für Luft- und Raumfahrt), Cologne, Germany; [c]Department of Mechanical and Aerospace Engineering, New Mexico State University, Las Cruces, NM, USA; [d]Metallic Structures and Materials Systems for Aerospace Engineering, RWTH Aachen University, Aachen, Germany; [e]Institute of Physics and Astronomy, University of Potsdam, Potsdam, Germany

ABSTRACT

The micromechanical behavior of an annealed Ti-6Al-4V material produced by Laser Powder Bed Fusion was characterized by means of in-situ synchrotron X-ray diffraction during a tensile test. The lattice strain evolution was obtained parallel and transversal to the loading direction. The elastic constants were determined and compared with the conventionally manufactured alloy. In the plastic regime, a lower plastic anisotropy exhibited by the lattice planes was observed along the load axis (parallel to the building direction) than in the transverse direction. Also, the load transfer from α to β phase was observed, increasing global ductility of the material. The material seems to accumulate a significant amount of intergranular strain in the transverse direction.

ARTICLE HISTORY

Received 21 October 2021
Accepted 5 April 2022

KEYWORDS

Additive manufacturing; Ti-6Al-4V; anisotropy; synchrotron X-ray diffraction; intergranular strain

1. Introduction

Metal additive manufacturing (AM) is nowadays used in various industrial applications (Herzog, Seyda, Wycisk, & Emmelmann, 2016). In fact, the Laser Powder Bed Fusion (LPBF) AM technique allows producing near-net shape structures and reducing the machining post-processing costs.

CONTACT Tatiana Mishurova ✉ tatiana.mishurova@bam.de Bundesanstalt für Materialforschung und–prüfung (BAM; Federal Institute for Materials Research and Testing), Unter den Eichen 87, Berlin, 12205, Germany.

However, there are a few factors, such as manufacturing defects (Sanaei, Fatemi, & Phan, 2019), residual stress (Mishurova, Artzt, Haubrich, Requena, & Bruno, 2019), and heterogeneity of microstructure (Barriobero-Vila et al., 2020) limiting the production of the reliable LPBF components (Kok et al., 2018).

The microstructure of LPBF materials is unique due to the complex thermal cycles which the material undergoes during production. The directional heat dissipation during the process often causes epitaxial grain growth and, thus, strong crystallographic texture (Simonelli, Tse, & Tuck, 2014). The texture usually results in the anisotropy of the mechanical properties (Agius, Kourousis, Wallbrink, & Song, 2017). Typically, LPBF Ti-6Al-4V in the as-built condition presents fine α/α′ laths (HCP) inside prior β grains (BCC) (Yang et al., 2018). This type of microstructure usually leads to a brittle behavior of the material (Thijs, Verhaeghe, Craeghs, Humbeeck, & Kruth, 2010). Therefore, a modification of the as-built microstructure after the laser melting is necessary to tune the mechanical performance. This goal can be accomplished by exploiting the laser energy during processing itself (i.e., “intrinsically” generating a heat treatment) during production (Barriobero-Vila et al., 2017) or annealing heat treatments after production (Zhang et al., 2018). However, as shown in (Vilaro, Colin, & Bartout, 2011), a single step annealing heat treatment above the β-transus temperature ($T_\beta \approx 995\,°C$) can reduce the ultimate tensile strength due to a rapid coarsening of β-grains. Therefore, sub-transus temperature heat treatments are of particular interest (Haubrich et al., 2019; Ter Haar & Becker, 2021). Additional to microstructural modification, annealing after manufacturing releases tensile residual stress often present in LPBF parts, and thus, improves mechanical performance (Mishurova et al., 2021).

In-situ synchrotron X-ray diffraction (SXRD) or neutron diffraction experiments during compression/tension are the perfect tools for the evaluation of the elastic and plastic anisotropy of materials as well as the intergranular stresses (Cho, Dye, Conlon, Daymond, & Reed, 2002; Daymond, 2004). In this case, the plastic anisotropy is discussed as the anisotropy exhibited by the lattice planes in each loading direction and not the macroscopic anisotropy in the radial or axial directions. In-situ SXRD investigation of a Ti-6Al-4V forged bar (Stapleton et al., 2008) allowed the estimation of the intergranular strains for several crystallographic planes of α-Ti. In Daymond and Bonner (2003) the lattice strain evolution in IMI-834 alloys (Ti-based) showed the presence of intergranular stress for every crystallographic plane at least in one of the directions (parallel or orthogonal to the load axis). Such difference between directions makes the prediction of the mechanical multiaxial behavior at least complicated.

A few studies have been performed to investigate the micromechanical behavior of AM Ti-6Al-4V. In our previous work, we showed that the diffraction elastic constant (DEC) of LPBF Ti-6Al-4V is larger than for conventionally produced material (Mishurova et al., 2020). Voisin et al. (2018) studied the effect of build orientation on mechanical behavior of LPBF Ti-6Al-4V. Their work highlighted that the onset of plasticity for some crystallographic orientations is smaller than that the material as a whole (i.e., macroscopic). This has been connected to the presence of residual stress. Sofinowski et al. (2019) reported some load transfer from the α lamellae to the martensitic regions in water quenched Electron Beam Melted Ti-6Al-4V. Zhang et al. (2020) compared the micromechanical behavior of Ti-6Al-4V LPBF materials with different heat treatments. They highlighted that the decrease of the stress concentration inside in the β-phase (by its coarsening and increase of volume fraction due to high temperature heat treatment) increases the ductility of the material.

From the debate in the literature, it is clear that the understanding of the deformation behavior and load transfer/partition of the material is needed if one wants to control and tailor the mechanical properties of LPBF Ti-6Al-4V. In this work, we investigate the micromechanical behavior of annealed LPBF Ti-6Al-4V by means of in-situ SXRD during tensile testing.

2. Material and methods

2.1. Materials

A LPBF Ti-6Al-4V cylinder (8 mm in diameter, 95 mm in length) was printed on a Ti-6Al-4V base plate (preheated to 200 °C) with the use of support structures and with its longitudinal axis along the build direction. An SLM Solutions 280^{HL} machine was employed to process plasma atomized Ti-6Al-4V ELI (grade 23) powder from AP&C with a particle size of $d_{90}<50\,\mu m$. The characterization of the powder has been reported elsewhere (Thiede et al., 2019). The process parameters were set to the following: laser power of 175 W, laser velocity of 500 mm/s, hatch distance of 100 µm and layers thickness of 30 µm. The chess scanning strategy was used with field size of 5 mm and rotating 90° from layer to layer. These manufacturing conditions were optimized in order to achieve minimum porosity and acceptable residual stress (see, e.g., Mishurova et al., 2019; Kasperovich, Haubrich, Gussone, & Requena, 2016). A heat treatment at 650 °C for 3 hours (i.e., stress relieving (Mishurova et al., 2017)) followed by 900 °C for 2 hours was performed in Argon atmosphere, with heating and cooling rates of around 7 °C/min. After the heat treatments the sample was machined (by turning) to the tensile specimen geometry presented in Figure 1.

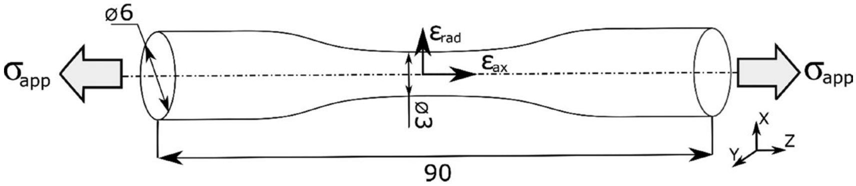

Figure 1. Schematic representation of the tensile specimen. The dimensions are in mm.

2.2. In-situ synchrotron energy dispersive X-ray diffraction

The *in-situ* SXRD during tensile test was conducted at EDDI beamline (HZB, Berlin, Germany) (Genzel, Denks, Gibmeier, Klaus, & Wagener, 2007). For the measurements energy dispersive (ED) diffraction in transmission mode was used. The aperture size of the primary and the secondary slits was 1 mm × 1 mm and 100 µm × 5 mm (equatorial × axial), respectively. For the tensile test a load rig (Walter + Bai AG) with maximum load of 20 kN, mounted on an Eulerian cradle, was employed. For each load step, the lattice strain ε was measured in axial (i.e., along the loading axis, ε_{ax}) and radial (i.e., perpendicular to loading axis, ε_{rad}) directions (Figure 1). The counting time was 2 minutes per spectrum. The load control was used in the elastic regime, with loading rate of 10 N/s. In the plastic regime (for applied stresses larger than 700 MPa) displacement control was used, with a displacement rate of 0.005 mm/s. The energy dispersive diffraction technique allows obtaining simultaneously the signal from several crystallographic planes *{hkl}* at a different energy:

$$d^{hkl}\left(\text{Å}\right)=\frac{6.199}{\sin\theta}\frac{1}{E^{hkl}(\text{keV})} \tag{1}$$

where d^{hkl} is the lattice spacing for crystallographic plane *{hkl}*, θ is the Bragg's angle, E^{hkl} is the energy of X-ray beam corresponding to the crystallographic plane *{hkl}*. The lattice strain for different crystallographic planes ε^{hkl}, was calculated from lattice spacing d^{hkl} for every step as

$$\varepsilon^{hkl}=\frac{d^{hkl}-d_{in}^{hkl}}{d_{in}^{hkl}} \tag{2}$$

Strain-free reference d_{in}^{hkl} was defined as the lattice spacing at pre-load (with applied stress around 10 MPa, clamps force).

2.3. Microstructural characterization and texture analysis

The microstructure was characterized in the top part of the tensile sample (clamped region during the tensile test). The measurements were performed in the plane perpendicular to the build direction. The sample was ground and then polished with an aqueous suspension of 0.04 µm SiO_2 particles with an addition of 10% H_2O_2. Scanning electron microscopy (SEM) was conducted in backscattered electron mode (BSE) on a LEO 1530VP microscope with Gemini tower (Zeiss). The operation voltage was 15 kV and the working distance of 7 mm.

Texture analysis was also performed in the ED diffraction mode, employing the ED laboratory diffractometer LEDDI (HZB, Berlin, Germany). LEDDI features are described in detail in (Apel et al., 2018). The texture measurements were conducted in reflection geometry. A conventional tungsten X-ray tube with long fine-focus was operated at U = 60 kV and I = 45 mA in combination with an ED detector system. The latter allows the simultaneous collection of multiple diffraction lines *hkl* up to photon energies of 60 keV in a single spectrum, recorded under an arbitrary but fixed Bragg angle 2θ. For texture analysis, ED spectra were acquired at azimuthal angles φ (rotation in the XY plane, see Figure 1) and the inclination angles ψ (tilting in the XZ plane) in the intervals $\varphi \in [0°; 355°]$ and $\psi \in [0°; 85°]$ in steps of 5°. The texture measurements were performed in the plane perpendicular to the build direction, at the same location where microscopy was carried out. From six *hkl* reflections of α/α′-Ti the orientation distribution function (ODF) was evaluated. From the ODF, pole figures for all crystallographic plane families {*hkl*} could be calculated. The ODF as well as the recalculated pole figures were processed using the software package LaboTex 3.0 (Pawlik & Ozga, 1999).

From the texture measurements the average (or equivalent) elastic strain $<\varepsilon>$ (as proposed by Daymond (2004) and also shown in Mishurova et al. (2020)) was calculated as

$$<\varepsilon> = \frac{\sum_{hkl} \varepsilon_{hkl} f_{hkl}}{\sum_{hkl} f_{hkl}} \tag{3}$$

where f_{hkl} is the fraction of grains with orientation {*hkl*}. This fraction depends on the direction inside the specimen, i.e., on the angle ψ of the specimen inclination to the scattering vector. The function $f_{hkl}(\psi)$ can be extracted from the recalculated pole figures, Figure 3. Calculated inverse pole figures of α-Ti using the texture intensity ($I_{hkl}(\psi)$) of every reflection and weighting it by its multiplicity *mhkl* (note that six peaks were used for this calculation):

$$f_{hkl}(\psi) = \frac{I_{hkl}(\psi)\, m_{hkl}}{\sum_{hkl=1}^{6} I_{hkl}(\psi) \cdot m_{hkl}} \tag{4}$$

Since the material presented a fiber texture, the pole figures could be integrated along φ, and the ODF depended only on the angle ψ. This calculation yielded the dependence of $f_{hkl}(\psi)$ as a function of tilt angle with respect to the sample long direction, or in other words the azimuthal distribution of the fractions of a crystallite family from the axial to the radial directions, also shown in Mishurova et al. (2020).

3. Results and discussion

The material presents an α + β microstructure, where the β phase appears at the interfaces of the α lamellae (Figure 2a). According to quantitative image analysis, the average thickness of the α laths is around 3 µm. Figure 2b shows the diffraction patterns obtained prior to the tensile test by *in-situ* SXRD for different ψ tilt angles. The changes in peak intensity for each ψ are evidence of strong crystallographic texture. The texture is also present in the β phase (only β-200 reflection was detected). Usually, the crystallographic texture influences the plastic anisotropy among crystallographic plane due to the change of the relative volume fraction of grains with specific orientations with respect to a random texture.

The calculated pole figures of α-Ti obtained in the build plane by XRD (plane perpendicular to building direction) for the specimen are presented in Figure 3. The pole figures indicate a double fiber texture (with fiber axes {102} and {110}). Similar texture poles have also been reported for as-built material (without heat treatment (Mishurova et al., 2020; Mishurova, Bruno, Evsevleev, & Sevostianov, 2020)). However, the

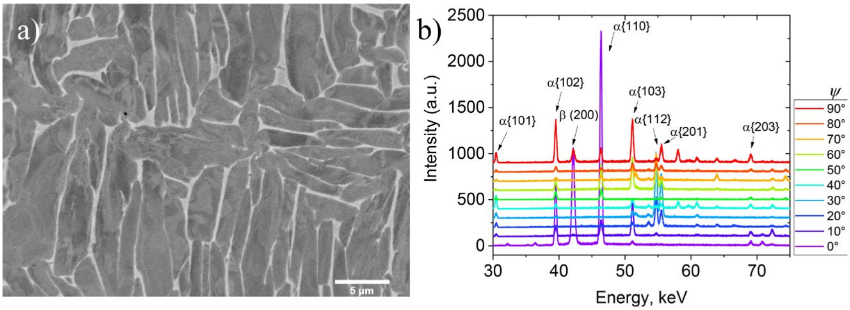

Figure 2. (a) BSE-SEM image taken from build plane (XY) and (b) the diffraction patterns obtained by SXRD experiment prior the loading for different tilt angles ψ.

maximum intensity of the texture slightly decreases with annealing (7.5× that of a random grain orientation for the as-built (Mishurova, Bruno, et al., 2020) and 5× random for the heat treatment condition presented in this study).

The macroscopic stress-relative displacement curve, acquired during the *in-situ* tensile test, is shown in Figure 4. The macroscopic yield stress occurs at around 800 MPa. Since the macrostrain was not measured by a strain gauge, a precise quantitative analysis of the stress-strain curve is not possible.

The evolution of lattice strains with applied stress is presented in Figure 5. For the determination of elastic properties, the *stress-microstrain conversion tensor (SμECT)* A_{ijkl} was introduced (in this case analogue to DEC) in Mishurova et al. (2020) and Mishurova, Bruno, et al., (2020). The SμECT connects the elastic response of an individual grain with the *effective* (macroscopic) strain of the specimen (material surrounding the grain):

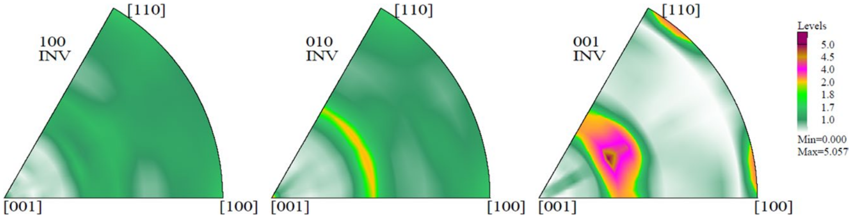

Figure 3. Calculated inverse pole figures of α-Ti.

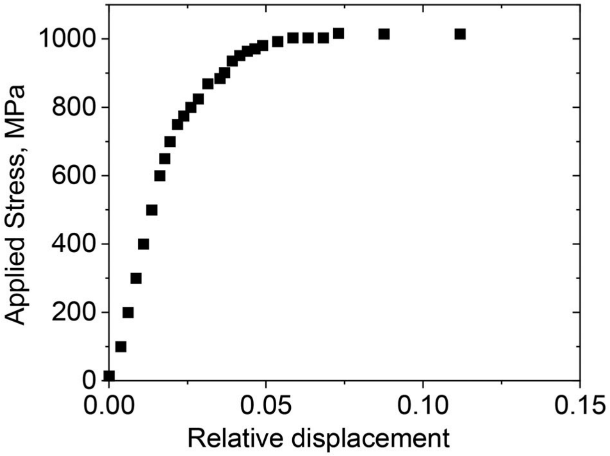

Figure 4. Macroscopic stress vs. relative displacement curves obtained during the in-situ tensile test.

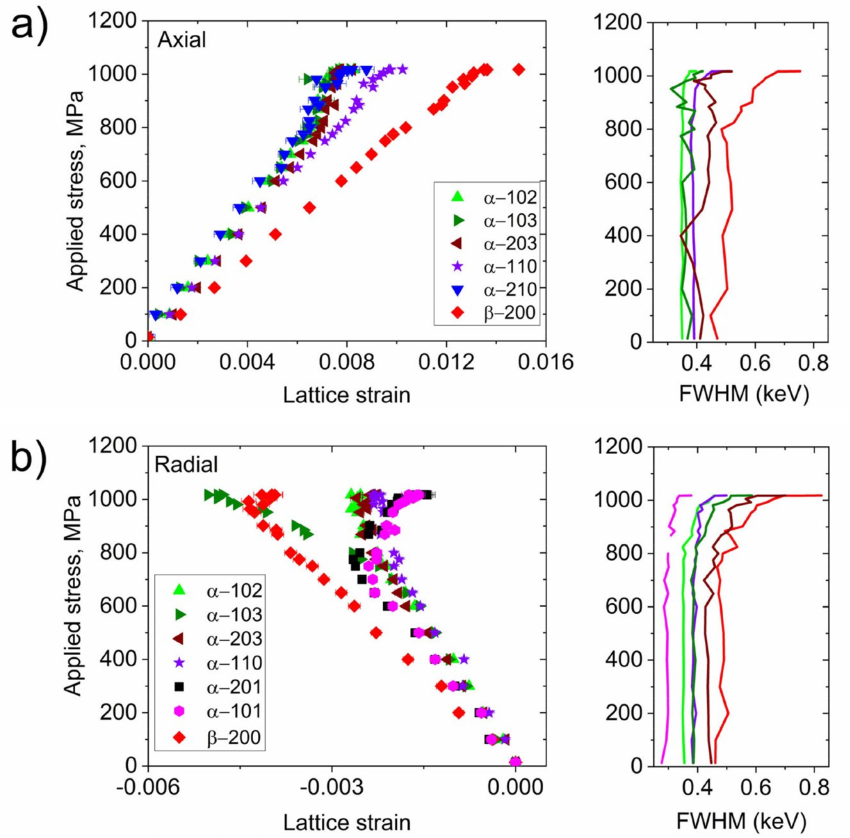

Figure 5. Applied Stress vs. lattice strain and FWHM for (a) axial direction; (b) radial direction.

$$< \varepsilon_{ij} >_{micro} = < A_{ijkl} > \sigma_{kl} \tag{5}$$

From the elastic part of the curve (up to 600 MPa) the inverse of the component of *SμECT* along the axial direction (A_{ax}^{-1}) was calculated and compared with the results for as-built LPBF and forged Ti-6Al-4V (Table 1). The elastic properties are mostly similar for as-built and heat treated LPBF Ti-6Al-4V, despite the microstructural modification by the heat treatment (a partially martensitic α + α′ appears for the as-built, while an α + β microstructure appears after heat treatment, see Figure 2a). Interestingly, A_{ax}^{-1} for the α phase in LPBF materials is larger than for forged Ti-6Al-4V, for both as-built and annealed (Stapleton et al., 2008). This is not the case for the β phase, in which the elastic modulus is similar for the forged bar and the annealed LPBF samples. In the two

Table 1. A_{ax}^{-1} (GPa) for different *hkl* reflections.

	102-α	103-α	203-α	110-α	210-α	200-β
This study	122.5 ± 1.5	115.6 ± 4.9	115.9 ± 3.9	105.1 ± 0.9	124.3 ± 4.1	76.5 ± 1.1
As-built LPBF (Mishurova et al., 2020)	120.1 ± 2.5	125.3 ± 1.5	115.8 ± 1.9	110.0 ± 1.1	107.8 ± 1.5	–
Forged bar (Stapleton et al., 2008)	106	106	–	96	–	78

cases the β phase (current study and (Stapleton et al., 2008)) appears at the α grain boundaries, which can explain similarity in behavior.

The macroscopic yield stress is similar to the microscopic one for the axial direction: most of α-Ti reflections (except α-110) start to deviate from the linear behavior at around 800 MPa (Figure 5a). Normally, different crystallographic families possess a different onset of plasticity; due to the different orientation of grains with respect to the loading direction, because they have a different Schmidt factor. Thus, as also reported in Voisin et al. (2018), the onset of plasticity for α-{110} crystallographic plane (of LPBF Ti-Al-4V) is lower than expected from macroscopic behavior. In the present case, the α-110 reflection shows *the least* plastic anisotropy (Figure 5a). In contrast, the other reflections present the onset of plasticity at around 700 MPa in the radial direction. It should be noticed, that in the radial direction the applied stress is compressive, so that the plastic behavior can be very different from the axial direction. The information about basal {002} and prismatic {100} planes would be beneficial for the understanding of the load partition between the orientations. However, due to the crystallographic texture (Figure 3) these reflections could not be detected.

Interestingly, the β-phase (in both directions) follows a fairly linear behavior even after the macroscopic yield point (Figure 5a). At this point most of α-Ti reflections do not increase the lattice strain anymore, thus the load transfer from α to β-phase takes place. However, the beginning of plastic deformation in β-phase is also evidenced by the increase of FWHM of the β-200 peak (starting at the onset of macroscopic plasticity, i.e., around 800 MPa). The β phase (BCC) has more slip systems than α (HCP) and, therefore, the presence of β improves the ductility in α + β alloys. Thus, the β-phase allows accumulating significant lattice strain compared to α phase.

When plotting the lattice strain evolution as a function of applied displacement, the plastic part of the curves appears clearer (Figure 6). The lattice strain of all visible reflections remains practically constant for relative displacements > 0.006. A large difference in the plastic behavior among

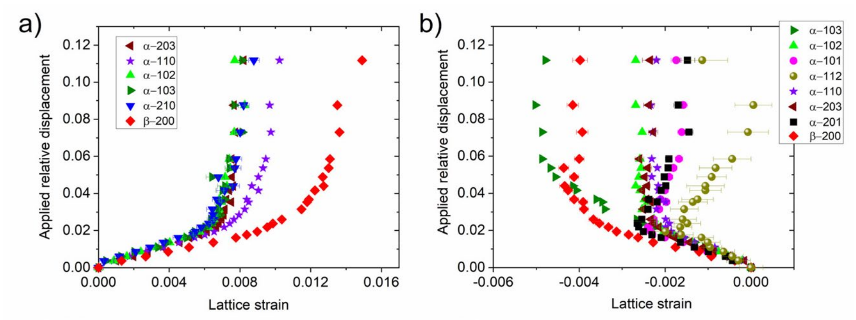

Figure 6. Applied relative displacement vs. lattice strain curved in (a) axial and (b) radial directions.

different grain families of α phase is visible in the radial direction (i.e., under compression), while most of the reflections behave similarly along the axial direction (tension). Although twinning is almost completely suppressed in α + β Ti alloys due to high solute content (Lütjering & Williams, 2007), activation of twinning was observed in conventional (Wielewski, Siviour, & Petrinic, 2012) and LPBF Ti-6Al-4V (Vallejos et al., 2021; Voisin et al., 2018). In the HCP systems the most commonly activated twinning systems are {101} and {112} under compression, and {102} and {111} under tension (Christian & Mahajan, 1995). Indeed, the current measurement shows that for the radial direction (i.e., in compression) the planes {101} and {112} undergo a decrease of the lattice strain (i.e., "unloading") after reaching the yield point (Figure 6b). This could be related to the activation of compression twinning. Such behavior is not observed in tension (axial direction). Vallejos at el. (2021) highlighted that the activation of the twinning system in LPBF Ti6Al4V depends on the orientation of the building directions with respect to the loading (i.e., crystallographic texture).

The plastic intergranular strains (ε^{p}_{is}) were estimated by the calculation of the plastic lattice strain after (virtual) linear unloading, applying the slope obtained in the elastic part (up to 600 MPa, A^{-1}_{ax}), according to

$$\begin{aligned}\varepsilon^{p}_{is,ax} &= \varepsilon^{hkl}_{ax} - A^{hkl}_{ax}\sigma_{app}\\ \varepsilon^{p}_{is,rad} &= \varepsilon^{hkl}_{rad} - A^{hkl}_{rad}\sigma_{app}\end{aligned} \tag{6}$$

Results of the plastic intergranular strain calculation are presented in Figure 7. In the axial direction the difference between reflections is not large and most values lay in the range from −0.001 to 0.001 (Figure 7a). The α-110 reflection shows the smallest intergranular strains, i.e., the smallest deviation from linear behavior (Figure 7b). As far as β-phase is concerned, only the last point (σ_{app}=1020 MPa) shows a plastic strain

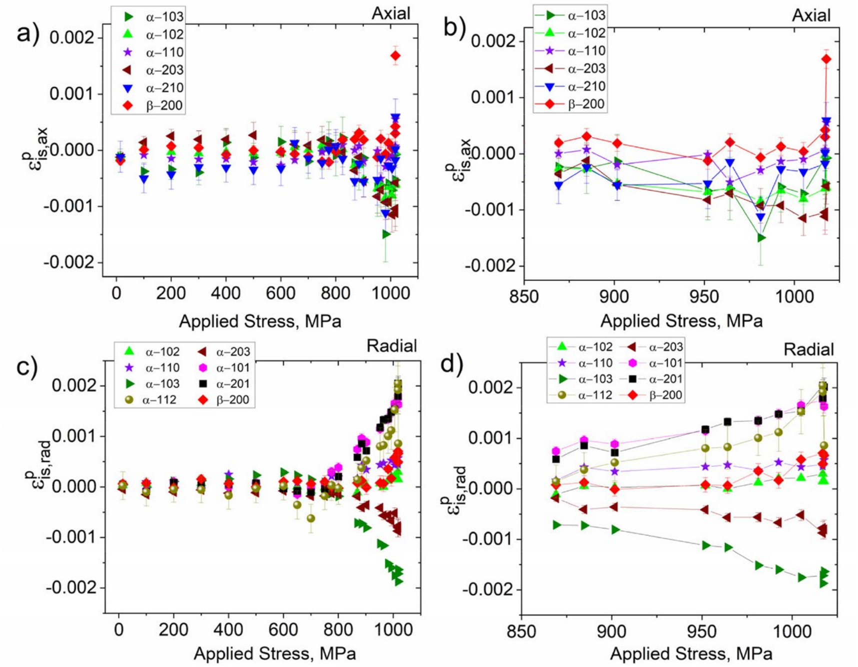

Figure 7. Intergranular strains in (a) axial direction, (b) axial direction plastic regime (zoom of (a)), (c) radial direction, (c) radial direction plastic regime (zoom of (c)).

value larger than 0.002. In general, for most of the reflections, the intergranular strains in radial direction ($\varepsilon^{p}_{is,rad}$) present higher plastic anisotropy than in the axial direction.

Figure 8a presents the comparison between the intergranular plastic strain of LPBF Ti-6Al-4V and the same alloy produced by ingot metallurgy followed by forging (the latter reported by Stapleton et al. (2008)). In order to compare the residual strains, the orientation parameter H^2 is introduced as

$$H^2 = \frac{l^2}{\frac{4}{3}\left(\frac{c}{a}\right)^2\left(h^2+k^2+hk\right)+l^2} \tag{7}$$

The evolution of the intergranular plastic strain of the α phase is very similar for the two materials. The residual lattice strains as a function of H^2 have also the same tendency (Figure 8b). In contrast, the β-phase accumulated much more plastic strain in the conventional material compared to the LPBF material.

The knowledge of the intergranular strain is essential for quantitative residual stress analysis by means of diffraction techniques. At

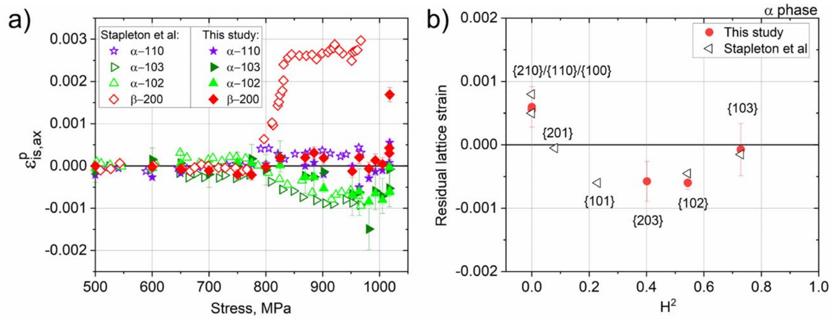

Figure 8. (a) Comparison of intergranular plastic strain along axial direction with forged bar Stapleton et al. (2008); (b) Residual lattice strain of α phase.

monochromatic sources (e.g., steady state neutron or monochromatic X-ray beams), the usual approach is to select reflections with low intergranular strains for strain analysis. Often the experimental setup and time restrictions do not allow the acquisition of more than one reflection. Typically, pyramidal HCP orientation (such as {102} or {103}) are recommended for residual stress analysis (ISO Standard 21432 2019). Cho et al. (2002) reported that none of the reflections mentioned above showed suitable intergranular strain for macrostress analysis in a IMI 834 alloy. Also, Daymond et al. (Daymond & Bonner, 2003) highlighted the challenge for the selection of reflection with the least intergranular stress in IMI 834, since the reflections that have linear behavior in axial direction do not behave linearly in the radial direction. Similar results are obtained in the present study for annealed LPBF Ti-6Al-4V (Figure 7). In the axial direction all α reflections show similar intergranular plastic strains, while in the radial direction there are clear differences in the accumulation of plastic strain between the different planes.

4. Summary

In this study the micromechanical behavior of annealed LPBF Ti-6Al-4V material was investigated by means of in-situ SXRD tensile test. Along the axial direction most of measured crystallographic planes of α-Ti showed similar behavior, with the α-110 reflection exhibiting the lowest plastic anisotropy (i.e., non-linear strain behavior). In the radial direction, a pronounced difference between the microstrain evolutions was observed between the planes, where the activation of compression twinning may play a role. In the plastic regime some load transfer from α to β phase was observed, increasing global ductility of the material. In the axial direction the material showed insignificant accumulation of intergranular strains (comparable to forged Ti6Al4V), while in the radial direction a higher plastic anisotropy led to higher intergranular strain for α-Ti.

Acknowledgement

The authors would like to thank Manuela Klaus, Christoph Genzel and Matthias Meixner from Helmholtz Zentrum Berlin for the support during experiment.

Data availability

The data that support the findings of this study are available from the corresponding author upon reasonable request.

Disclosure statement

The authors declare that there are no conflicts of interest of competing interested in the work presented above.

Notes on contributors

Tatiana Mishurova, Dr.-Ing., Postdoc at Bundesanstalt für Materialforschung und–prüfung (BAM), Division of Micro-Nondestructive Testing, Berlin. Research interest: metal additive manufacturing, material characterization, residual stress analysis.

Sergei Evsevleev, M. Sc, a PhD student at Bundesanstalt für Material for schung und–prüfung (BAM), Division of Micro-Nondestructive Testing, Berlin. Research interest: material characterization, image processing, computed tomography, machine learning.

Katia Artzt Dr.-Ing., research associate at the German Aerospace Center in Cologne. Research interest: metal additive manufacturing, material characterization, process monitoring.

Jan Haubrich, Dr. rer nat., head of the research group "Materials Engineering & Design" at the Deperatment of "Metallic and Hybrid Materials" of the Institute of Materials Research of the German Aerospace Center in Cologne. Research interest: metal additive manufacturing, surface treatments for bonding, material und surface characterization, dynamic processes on surfaces and in materials.

Guillermo Requena, Prof. Dr., Institute of Materials Research - German Aerospace Center / Metallic Structures and Materials Systems for Aerospace Engineering - RWTH Aachen University. Research Interest: Microstructure-Properties relationships in structural metals / Additive manufacturing of metals / 3D-imaging and diffraction to investigate materials under manufacturing and service conditions.

Igor Sevostianov, Prof. Dr, Professor of Mechanical Engineering, New Mexico State University, Las Cruses, USA. Research Interest: micromechanics of materials, cross-property connections, effective properties.

Giovanni Bruno, Prof. Dr, head of the Division of Micro- Nondestructive Testing at Bundesanstalt für Materialforschung und–prüfung (BAM)/Professor at Potsdam University, Research Interest: materials characterization, alloys, composites, residual stress analysis, computed tomography, mechanical properties, porosity.

ORCID

Giovanni Bruno http://orcid.org/0000-0001-9632-3960

References

Agius, D., Kourousis, K. I., Wallbrink, C., & Song, T. (2017). Cyclic plasticity and microstructure of as-built SLM Ti-6Al-4V: The effect of build orientation. *Materials Science and Engineering: A*, *701*, 85–100.

Apel, D., Meixner, M., Liehr, A., Klaus, M., Degener, S., Wagener, G., … Scholtes, B. (2018). Residual stress analysis of energy-dispersive diffraction data using a two-detector setup: Part II—Experimental implementation. *Nuclear Instruments and Methods in Physics Research Section A: Accelerators, Spectrometers, Detectors and Associated Equipment*, *877*, 56–64.

Barriobero-Vila, P., Artzt, K., Stark, A., Schell, N., Siggel, M., Gussone, J., … Haubrich, J. (2020). Mapping the geometry of Ti-6Al-4V: From martensite decomposition to localized spheroidization during selective laser melting. *Scripta Materialia*, *182*, 48–52.

Barriobero-Vila, P., Gussone, J., Haubrich, J., Sandlöbes, S., Da Silva, J., Cloetens, P., … Requena, G. (2017). Inducing stable α + β microstructures during selective laser melting of Ti-6Al-4V using intensified intrinsic heat treatments. *Materials*, *10*(3), 268.

Cho, J. R., Dye, D., Conlon, K. T., Daymond, M. R., & Reed, R. C. (2002). Intergranular strain accumulation in a near-alpha titanium alloy during plastic deformation. *Acta Materialia*, *50*(19), 4847–4864.

Christian, J. W., & Mahajan, S. (1995). Deformation twinning. *Progress in Materials Science*, *39*(1–2), 1–157.

Daymond, M. R. (2004). The determination of a continuum mechanics equivalent elastic strain from the analysis of multiple diffraction peaks. *Journal of Applied Physics*, *96*(8), 4263–4272.

Daymond, M. R., & Bonner, N. W. (2003). Lattice strain evolution in IMI 834 under applied stress. *Materials Science and Engineering: A*, *340*(1–2), 272–280.

Genzel, C., Denks, I. A., Gibmeier, J., Klaus, M., & Wagener, G. (2007). The materials science synchrotron beamline EDDI for energy-dispersive diffraction analysis. *Nuclear Instruments and Methods in Physics Research Section A: Accelerators, Spectrometers, Detectors and Associated Equipment*, *578*(1), 23–33.

Haubrich, J., Gussone, J., Barriobero-Vila, P., Kürnsteiner, P., Jägle, E. A., Raabe, D., … Requena, G. (2019). The role of lattice defects, element partitioning and intrinsic heat effects on the microstructure in selective laser melted Ti-6Al-4V. *Acta Materialia*, *167*, 136–148.

Herzog, D., Seyda, V., Wycisk, E., & Emmelmann, C. (2016). Additive manufacturing of metals. *Acta Materialia*, *117*, 371–392.

Hielscher, R., & Schaeben, H. (2008). A novel pole figure inversion method: Specification of the MTEX algorithm. *Journal of Applied Crystallography*, *41*(6), 1024–1037.

ISO Standard 21432. (2019). Non-destructive testing - Standard test method for determining residual stresses by neutron diffraction. Gevena, Switzerland: ISO, in press.

Kasperovich, G., Haubrich, J., Gussone, J., & Requena, G. (2016). Correlation between porosity and processing parameters in TiAl6V4 produced by selective laser melting. *Materials & Design*, *105*, 160–170.

Kok, Y., Tan, X. P., Wang, P., Nai, M. L. S., Loh, N. H., Liu, E., & Tor, S. B. (2018). Anisotropy and heterogeneity of microstructure and mechanical properties in metal additive manufacturing: A critical review. *Materials & Design*, *139*, 565–586.

Lütjering, G., & Williams, J. C. (2007). *Titanium*. Berlin, Heidelberg: Springer-Verlag.

Mishurova, T., Artzt, K., Haubrich, J., Evsevleev, S., Evans, A., Meixner, M., … Bruno, G. (2020). Connecting diffraction-based strain with macroscopic stresses in laser powder bed fused Ti-6Al-4V. *Metallurgical and Materials Transactions A*, *51*(6), 3194–3204.

Mishurova, T., Artzt, K., Haubrich, J., Requena, G., & Bruno, G. (2019). New aspects about the search for the most relevant parameters optimizing SLM materials. *Additive Manufacturing*, *25*, 325–334.

Mishurova, T., Artzt, K., Rehmer, B., Haubrich, J., Avila, L., Schoenstein, F., … Bruno, G. (2021). Separation of the impact of residual stress and microstructure on the fatigue performance of LPBF Ti-6Al-4V at elevated temperature. *International Journal of Fatigue*, *148*, 106239.

Mishurova, T., Bruno, G., Evsevleev, S., & Sevostianov, I. (2020). Determination of macroscopic stress from diffraction experiments: A critical discussion. *Journal of Applied Physics*, *128*(2), 025103.

Mishurova, T., Cabeza, S., Artzt, K., Haubrich, J., Klaus, M., Genzel, C., … Bruno, G. (2017). An assessment of subsurface residual stress analysis in SLM Ti-6Al-4V. *Materials*, *10*(4), 348–362.

Pawlik, K., & Ozga, P. (1999). LaboTex: The texture analysis software, Goettinger Arbeiten zur Geologie und Palaeontologie SB4, 146–147.

Sanaei, N., Fatemi, A., & Phan, N. (2019). Defect characteristics and analysis of their variability in metal L-PBF additive manufacturing. *Materials & Design*, *182*, 108091.

Simonelli, M., Tse, Y. Y., & Tuck, C. (2014). On the texture formation of selective laser melted Ti-6Al-4V. *Metallurgical and Materials Transactions A*, *45*(6), 2863–2872.

Sofinowski, K., Šmíd, M., Kuběna, I., Vivès, S., Casati, N., Godet, S., & Van Swygenhoven, H. (2019). In situ characterization of a high work hardening Ti-6Al-4V prepared by electron beam melting. *Acta Materialia*, *179*, 224–236.

Stapleton, A. M., Raghunathan, S. L., Bantounas, I., Stone, H. J., Lindley, T. C., & Dye, D. (2008). Evolution of lattice strain in Ti–6Al–4V during tensile loading at room temperature. *Acta Materialia*, *56*(20), 6186–6196.

Ter Haar, G. M., & Becker, T. H. (2021). Low temperature stress relief and martensitic decomposition in selective laser melting produced Ti6Al4V. *Material Design & Processing Communications*, *3*(1), e138.

Thiede, T., Mishurova, T., Evsevleev, S., Serrano-Munoz, I., Gollwitzer, C., & Bruno, G. (2019). 3D shape analysis of powder for laser beam melting by synchrotron X-ray CT. *Quantum Beam Science*, *3*(1), 3.

Thijs, L., Verhaeghe, F., Craeghs, T., Humbeeck, J. V., & Kruth, J.-P. (2010). A study of the microstructural evolution during selective laser melting of Ti–6Al–4V. *Acta Materialia*, *58*(9), 3303–3312.

Vallejos, J. M., Barriobero-Vila, P., Gussone, J., Haubrich, J., Kelm, K., Stark, A., … Requena, G. (2021). In situ high-energy synchrotron X-ray diffraction reveals the role of texture on the activation of slip and twinning during deformation of laser powder bed fusion Ti–6Al–4V. *Advanced Engineering Materials*, *23*(11), 2001556.

Vilaro, T., Colin, C., & Bartout, J. D. (2011). As-fabricated and heat-treated microstructures of the Ti-6Al-4V alloy processed by selective laser melting. *Metallurgical and Materials Transactions A*, *42*(10), 3190–3199.

Voisin, T., Calta, N. P., Khairallah, S. A., Forien, J.-B., Balogh, L., Cunningham, R. W., … Wang, Y. M. (2018). Defects-dictated tensile properties of selective laser melted Ti-6Al-4V. *Materials & Design*, *158*, 113–126.

Wielewski, E., Siviour, C. R., & Petrinic, N. (2012). On the correlation between macrozones and twinning in Ti–6Al–4V at very high strain rates. *Scripta Materialia*, *67*(3), 229–232.

Yang, J., Yu, H., Yang, H., Li, F., Wang, Z., & Zeng, X. (2018). Prediction of microstructure in selective laser melted Ti 6Al 4V alloy by cellular automaton. *Journal of Alloys and Compounds*, *748*, 281–290.

Zhang, D., Wang, L., Zhang, H., Maldar, A., Zhu, G., Chen, W., … Zeng, X. (2020). Effect of heat treatment on the tensile behavior of selective laser melted Ti-6Al-4V by in situ X-ray characterization. *Acta Materialia*, *189*, 93–104.

Zhang, X.-Y., Fang, G., Leeflang, S., Böttger, A. J., Zadpoor, A. A., & Zhou, J. (2018). Effect of subtransus heat treatment on the microstructure and mechanical properties of additively manufactured Ti-6Al-4V alloy. *Journal of Alloys and Compounds*, *735*, 1562–1575.